A Numerical and Experimental Investigation of Sabot Separation Dynamics

M. Guillot and W. G. Reinecke
Institute for Advanced Technology
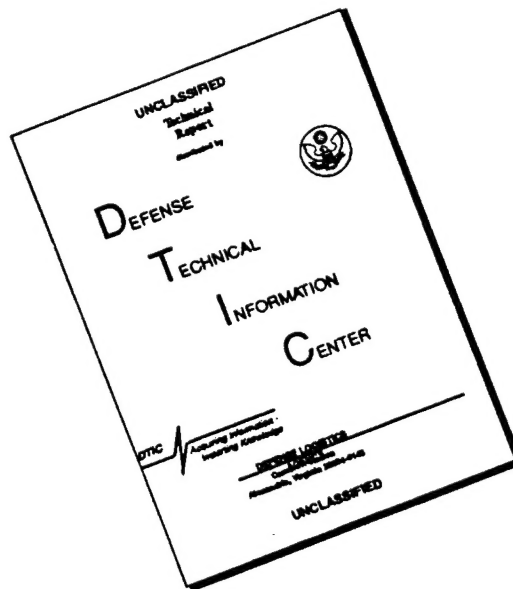*The University of Texas at Austin*

September 1995

DTIC QUALITY INSPECTED 2
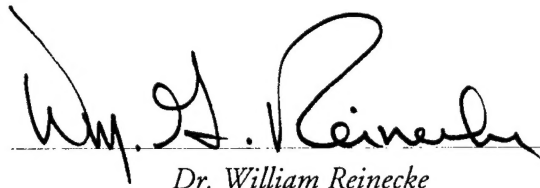
IAT.R 0074

19960917 016

DISCLAIMER NOTICE

THIS DOCUMENT IS BEST QUALITY AVAILABLE. THE COPY FURNISHED TO DTIC CONTAINED A SIGNIFICANT NUMBER OF PAGES WHICH DO NOT REPRODUCE LEGIBLY.

Certification of Technical Review

Dr. William Reinecke

Dr. Thomas Kiehne

REPORT DOCUMENTATION PAGE

Form Approved
OMB NO. 0704-0188

1. AGENCY USE ONLY (Leave blank)	2. REPORT DATE September 1995	3. REPORT TYPE AND DATES COVERED Technical Report

4. TITLE AND SUBTITLE
A Numerical and Experimental Investigation of Sabot Separation Dynamics

5. FUNDING NUMBERS
Contract # DAAA21-93-C-0101

6. AUTHOR(S)
M. Guillot and W. G. Reinecke

7. PERFORMING ORGANIZATION NAME(S) AND ADDRESS(ES)
Institute for Advanced Technology
The University of Texas at Austin
4030-2 W. Braker Lane, #200
Austin, TX 78759

8. PERFORMING ORGANIZATION REPORT NUMBER
IAT.R 0074

9. SPONSORING / MONITORING AGENCY NAME(S) AND ADDRESS(ES)
U.S. Army Research Laboratory
ATTN: AMSRL-WT-T
Aberdeen Proving Ground, MD 21005-5066

10. SPONSORING / MONITORING AGENCY REPORT NUMBER

11. SUPPLEMENTARY NOTES
The view, opinions and/or findings contained in this report are those of the author(s) and should not be considered as an official Department of the Army position, policy, or decision, unless so designated by other documentation.

12a. DISTRIBUTION / AVAILABILITY STATEMENT
Approved for public release; distribution unlimited.

12b. DISTRIBUTION CODE
A

13. ABSTRACT (Maximum 200 words)

A sabot trajectory analysis is performed on three hypervelocity kinetic energy penetrators using a modified version of a code developed to compute sabot discard trajectories. The code was modified from the original version to allow computed trajectories of more complicated sabot designs. Specifically, modifications were made to the front scoop geometry and associated aerodynamic model. The computed trajectories are compared to experimental data obtained in the Institute for Advanced Technology's Hypervelocity Launch Facility and to predictions made with the original version of the code to assess the overall accuracy of the code and the improvements of the modifications. Additionally, an analytical model is developed to verify the trends predicted by the computer code and to help identify possible improvements to the pressure modeling in the code.

14. SUBJECT TERMS
sabot discard, pressure distribution, sabots in hypervelocity flight

15. NUMBER OF PAGES
30

16. PRICE CODE

17. SECURITY CLASSIFICATION OF REPORT Unclassified	18. SECURITY CLASSIFICATION OF THIS PAGE Unclassified	19. SECURITY CLASSIFICATION OF ABSTRACT Unclassified	20. LIMITATION OF ABSTRACT UL

TABLE OF CONTENTS

LIST OF FIGURES

LIST OF TABLES

A Numerical and Experimental Investigation of Sabot Separation Dynamics

Martin J. Guillot, William G. Reinecke

1.0 INTRODUCTION

High acceleration loads transmitted to gun launched projectiles during the launch cycle require projectiles to be structurally supported while in-bore. This is even more critical for long rod penetrators under investigation today. The usual method for supporting projectiles in-bore is to use a sabot made of two or more petals which encases the projectile and provides the needed structural support for the projectile to withstand the acceleration loads. However, after the projectile has exited from the muzzle of the gun, the sabot must be removed from the projectile as quickly as possible to minimize aerodynamic drag. This is normally accomplished by designing the sabot so that aerodynamic forces strip the sabot petals from the projectile. Sabot separation is a highly complex and unsteady aerodynamic process, and if not accomplished properly can be a source of perturbing forces and moments that can result in an unacceptable level of dispersion. Therefore, a thorough understanding of sabot separation dynamics has been, and continues to be, an important area of research for the U.S. Army.

In an effort to develop the capability to predict sabot separation dynamics within the framework of a reasonably simple physical and computational model capable of rapid parametric predictions, the AVCO Systems Division, under contract to the U.S. Army Ballistics Research Laboratory, began developing a computer model in the late 1970's to use as a sabot design tool. This code has become known as the AVCO Sabot Separation Code. It was originally written to compute sabot separation for relatively simplified geometries. However, the innovative projectile designs and increasingly complicated sabot geometries under investigation today have limited the usefulness of the current version of the AVCO code when modeling these sabots. Additionally, the original AVCO code has undergone several modifications over the years by different research agencies. These modifications have been documented in a series of reports [1-6]. However, to the authors' knowledge, there is no single report that documents the theoretical development of the current version of the AVCO code entirely, nor provides a comprehensive user's manual. Therefore, the current effort was undertaken for two reasons. The first was to modify the original authors' version of the code to compute trajectories of more complicated sabot geometries under development today. The second was to provide comprehensive documentation and a user's manual for the current version of the code.

Both the modified and original versions of the AVCO code were run for sabots launched at the IAT Hypervelocity Launch Facility. The results of both versions of the code were compared to X-Ray and witness plate data of radial and angular displacement at specific downrange locations to assess the overall ability of the code to accurately predict the sabot trajectories, and to assess the improvements of the modifications to the original version of the code.

In addition to the modifications to the AVCO code, a relatively simple analytical model was developed to help verify the trends predicted by the AVCO code. The results of the analytical model are also compared to the experimental data and are used to identify possible further improvements to the aerodynamic model in the AVCO code.

1

2.0 THEORETICAL AND NUMERICAL FORMULATION OF AVCO CODE

2.1 Equations of Motion

The theoretical formulation of the model incorporated into the AVCO code was o   na
developed by Crimi and Siegelman [1]. In keeping with the intention to provide a single   np
hensive documentation of the AVCO code, and to provide the reader with a base refere   point
for the discussion of the modifications made in this study, the original formulation i: esented
here.

The basic equations of motion governing the sabot petal and projectile dynam s are the
conservation of linear momentum (Newton's second law) and the conservation of angular
momentum. These equations are written in an inertial coordinate system, (X,Y,Z), for each seg-
ment and, for asymmetric discard, the projectile. The inertial coordinate system is chosen such
that the origin is at the center of gravity of the projectile, which is assumed to move at constant
velocity. The centerline of the projectile lies along the X-axis with the positive direction toward
the projectile tip. See Figure 1. Also shown in the figure are body fitted coordinates used for
computing the aerodynamic forces. Initially, the X and z axes are aligned with each other. The
equations of motion are written in vector form as:

$$\sum \mathbf{F} = m\ddot{\mathbf{X}} \tag{1}$$

$$\sum \mathbf{M}_G = (\dot{\mathbf{H}}_G)_{xyz} + \omega \times \mathbf{H}_G \tag{2}$$

$(\dot{\mathbf{H}}_G)_{xyz}$ is the time rate of change of angular momentum measured in body fitted coordinates,
(x,y,z), ω is the angular velocity of the sabot segment measured in (X,Y,Z) coordinates, $\mathbf{H}_G$ is the
angular momentum of the segment, and the vector, $\mathbf{X}$, represents the three cartesian coordinate
components.

Equations (1) and (2) are sufficient to describe the motion of the sabot petals and projec-
tile. However, it is convenient to define additional variables, and to solve the equations in terms of
those variables. First, the rectangular components of the angular velocity, ω, are related to the
time rate of changes of Euler angles, (θ, ϕ, ψ), which are also shown in Figure 1. Referring to
the figure, it is easily seen that the rectangular components of angular velocity are related to the
time rate of change of the Euler angles by the matrix relation,

$$\begin{bmatrix} \cos\phi & \sin\theta\sin\phi & 0 \\ -\sin\phi & \sin\theta\cos\phi & 0 \\ 0 & \cos\theta & 1 \end{bmatrix} \begin{bmatrix} \dot{\theta} \\ \dot{\psi} \\ \dot{\phi} \end{bmatrix} = \begin{bmatrix} \omega_x \\ \omega_y \\ \omega_z \end{bmatrix} \tag{3}$$

Solving (3) for the Euler angles yields,
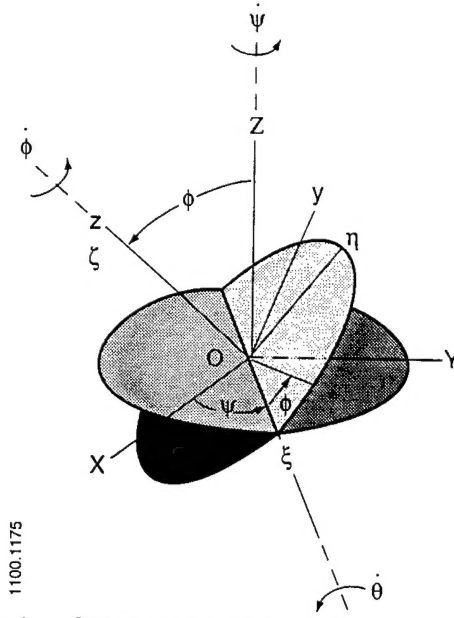
Figure 1. Sabot and inertial coordinate system.

$$\dot{\varphi} = \frac{\omega_x \sin\phi - \omega_y \cos\phi}{\sin\phi} \tag{4}$$

$$\dot{\theta} = \omega_x \cos\phi - \omega_y \sin\phi \tag{5}$$

$$\dot{\phi} = \omega_z - \cot\theta \, (\omega_x \sin\phi - \omega_y \cos\phi) \tag{6}$$

Second, the components of angular momentum with respect to the sabot petal center of gravity are given by the following matrix relation,

$$\begin{bmatrix} I_{xx} & 0 & 0 \\ 0 & I_{yy} & -I_{yz} \\ 0 & -I_{zy} & I_{zz} \end{bmatrix} \begin{bmatrix} \omega_x \\ \omega_y \\ \omega_z \end{bmatrix} = \begin{bmatrix} h_x \\ h_y \\ h_z \end{bmatrix} \tag{7}$$

Equation (7) is used to write the rectangular components of the angular velocity, ω, in terms of the components of angular momentum, (h_x, h_y, h_z), in equation (2) and equations (4) through (6). This yields a system of coupled equations given by equations (1) and (2), and (4) through (6). These equations are solved using the Runge-Kutta method, which is described in more detail in Section 3.0.

The aerodynamic forces are most easily evaluated in body fitted coordinates, but before they can be used in the above equations they must be transformed into inertial coordinates. The transformation is given by,

3

$$\begin{bmatrix} F_X \\ F_Y \\ F_Z \end{bmatrix} = \begin{bmatrix} T \end{bmatrix} \begin{bmatrix} F_x \\ F_y \\ F_z \end{bmatrix} \tag{8}$$

where, the transformation matrix $[T]$ is given by,

$$[T] = \begin{bmatrix} (\cos\phi\cos\psi - \sin\phi\cos\theta\sin\phi) & (-\sin\phi\cos\psi - \cos\phi\cos\theta\sin\psi) & (\sin') \\ (\cos\phi\sin\phi + \sin\phi\cos\theta\cos\psi) & (-\sin\phi\sin\psi + \sin\phi\cos\theta\cos\psi) & (-\sin\theta\cos\phi) \\ (\sin\theta\sin\phi) & (\sin\theta\cos\phi) & (\cos\theta) \end{bmatrix} \tag{9}$$

2.2 Aerodynamic Model

The original aerodynamic model developed for the AVCO code consists of two primary flow regimes. The first is when the sabot petals are in close proximity to one another and the forces and moments on each segment are influenced by the presence of the other petals, and by shock reflections and interactions. This is termed the interaction region. The second regime commences when each sabot petal is in free flight and not affected by the presence of the other sabot petals. In the interaction region, a relatively simple aerodynamic model based on inviscid 2-D gas dynamic relations is applied along the centerline of each sabot petal to determine the pressure distribution. Newtonian pressure distribution is assumed to exist when the sabot petals are in the free flight regime. Forces are computed using both the interaction region procedure and the Newtonian method at every point in the trajectory. Whenever the forces computed by the interaction method fall below those computed by the Newtonian method, the sabot petal is deemed to be in free flight and only Newtonian forces are computed thereafter. The sabot geometry modeled in the original AVCO code consists of a conical front scoop and a cylindrical body. The relevant geometric parameters are shown in Figure 2.
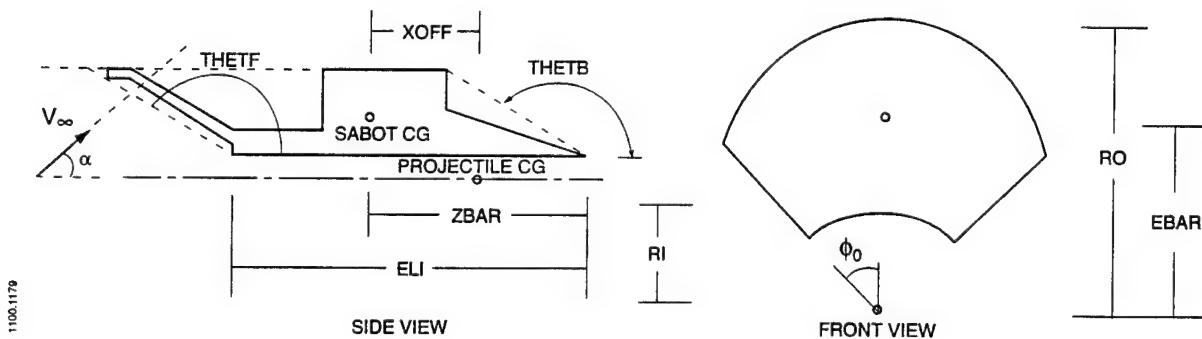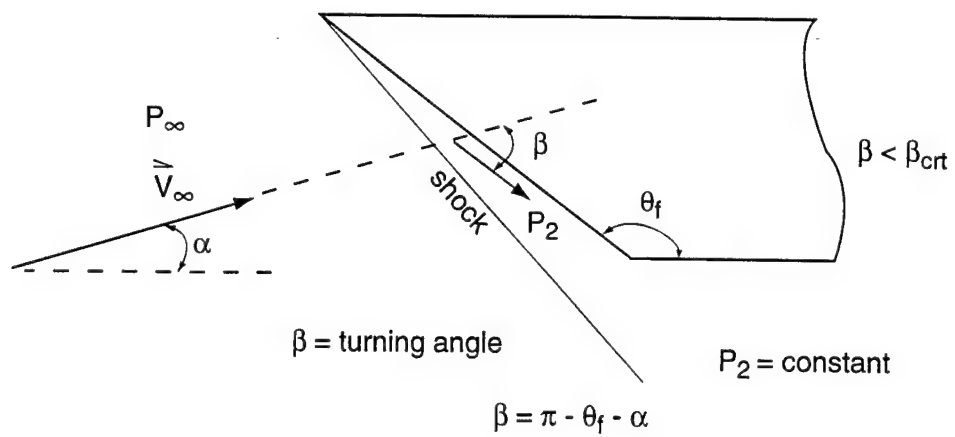

Figure 2.   Original sabot geometry model [5].

4

In the interaction region the pressure distribution is divided into two main areas of the sabot: the sabot front scoop and the sabot underside. On the front scoop, the procedure used to compute the pressure distribution depends on the angle of attack of the sabot. If the turning angle of the flow encountering the front scoop is small enough for an attached shock to exist, the pressure on the front scoop is assumed to be constant at the value behind the oblique shock. Planar shock relations are used. If the turning angle is greater than for an attached shock, the pressure on the front scoop is assumed to vary parabolically from stagnation at the outer radius to sonic at the inner radius. The two situations are sketched in Figures 3 (a) and (b). The base pressure level on the underside of the each sabot petal is computed by assuming that the flow turns through a Prandtl-Meyer expansion of angle $(\pi - \theta_f)$. However, the pressure along the underside of the sabot increases in the axial direction from the tip to the tail due to shock reflections and shock interactions. An approximate model based on empirical relations and experimental data by Schmidt [7] is used to approximate the pressure distribution. The experimental data indicate that a pressure pulse occurs on the underside of the sabot due to the interaction of the projectile bow shock and the reflection of the sabot bow shock off of the projectile. This pressure pulse is approximated by the procedure shown in Figure 4. A line from the sabot front scoop is extended parallel to the front scoop down to a point where it intersects the projectile. A Mach wave is then reflected back up to the sabot underside at the Mach wave angle, μ. This serves to define the beginning of the pressure pulse, S_b, and the end of the pressure pulse, S_e, as shown in the figure. The expressions for S_b and S_e are given by,

$$
S_b = -\frac{\delta \cos \theta_f}{\sin (\theta_f - \alpha)}
$$

$$
S_e = S_b + \frac{\delta \sin \theta_f}{\sin (\theta_f - \alpha)} \left[\frac{\cos \alpha \cot \mu - \sin \alpha}{\sin \alpha \cot \mu + \sin \alpha} \right]
$$

(10)

The pulse is assumed to be triangular with a peak halfway between S_b and S_e. The magnitude of the pressure pulse is determined from turbulent separation data.

5

P_∞

$\vec{V}_\infty$

α

β

shock

P_2

θ_f

$\beta < \beta_{crt}$

β = turning angle

P_2 = constant

$\beta = \pi - \theta_f - \alpha$

(a)

$P = P_{stag}$

β

$\beta > \beta_{crt}$

shock

θ_f

V_∞

α

$P_2 = P^*$
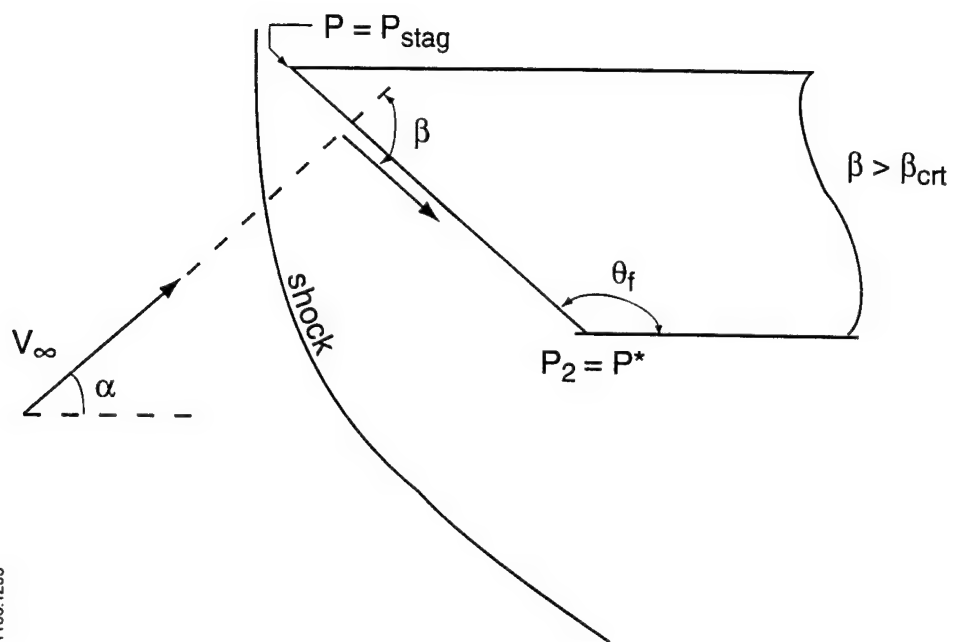
(b)

Figure 3. Original aerodynamic model.

6

θ_f

$\pi - \theta_f$

S_b S_e

Δ_s

δ

L L_2

α $\frac{\pi}{2} - (\alpha + \mu)$

θ_f-α

$\pi - (\theta_f - \alpha)$ μ

1100.1296

Figure 4. Location of pressure pulse on sabot underside.

The validity of this approach is discussed thoroughly by Crimi & Siegelman [2]. The authors compare the pressure distributions predicted by this model with experimental data. They achieve good agreement between their predictions and the experimental data. Based on this, they conclude that this approach, while having little theoretical basis, represents a valid empirical model.

3.0   MODIFICATIONS

In the current work, several modifications were made to the original formulation presented in Section 2.0. Briefly summarizing, they are:

- The Runge-Kutta algorithm was modified to allow any order Runge-Kutta scheme to be used. It is only necessary to input a table of coefficients through a user subroutine.

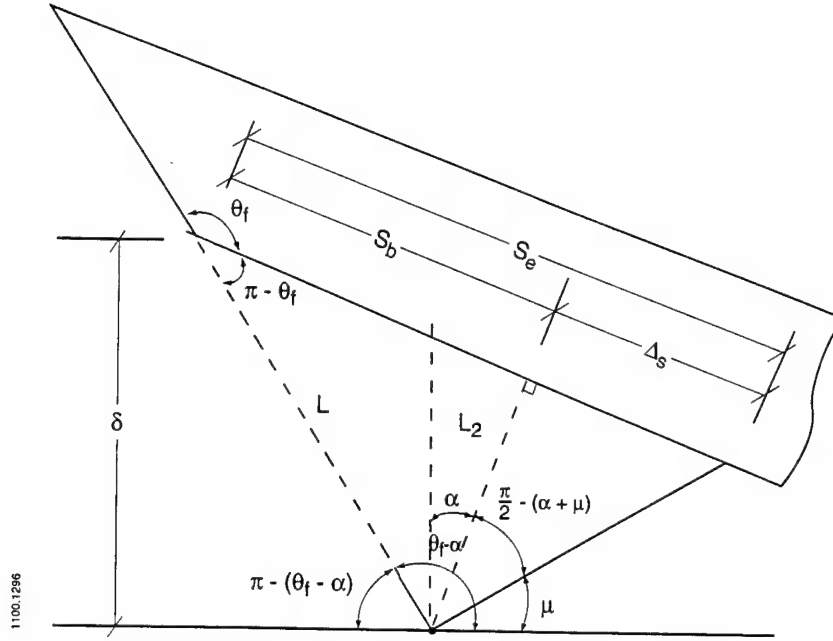- The error estimator and time-stepping scheme were improved so that the new time step is computed based on the error calculated.

- The Newtonian formulation was changed from straight Newtonian to modified Newtonian.

- The same side-face areas used to compute the forces and moments in the interaction region are now used to compute the forces and moments in the Newtonian regime.

- The front scoop geometry and aerodynamic model were modified so that the front scoop geometry can be modeled with one, two, or three line segments.

Each of these modifications is discussed in more detail below.

7

3.1   Runge-Kutta & Time Stepping Scheme

The equations presented in Section 2.1 are solved using the Runge-Kutta method. The equations are rewritten as a system of twelve first order differential equations by defining a vector $X_j = [X, Y, Z, \theta, \psi, \phi, \dot{\theta}, \dot{\psi}, \dot{\phi}, h_x, h_y, h_z]^T$, where $j = 1, ..., 12$. This yields a system of twelve equations for the twelve unknown variables which are written as:

$$\dot{X}_1 = X_4 \tag{11}$$

$$\dot{X}_2 = X_5 \tag{12}$$

$$\dot{X}_3 = X_6 \tag{13}$$

$$\dot{X}_4 = \frac{F_X}{m} \tag{14}$$

$$\dot{X}_5 = \frac{F_Y}{m} \tag{15}$$

$$\dot{X}_6 = \frac{F_Z}{m} \tag{16}$$

$$\dot{X}_7 = \left[\frac{X_{10}}{I_x} \sin(X_8) + \left[\frac{I_z X_{11} - I_{yz} X_{12}}{I_y I_z - I_{yz}^2} \right] \cos(X_8) \right] / \sin(X_9) \tag{17}$$

$$\dot{X}_8 = \left[\frac{X_{10}}{I_x} \cos(X_8) + \left[\frac{I_z X_{11} - I_{yz} X_{12}}{I_y I_z - I_{yz}^2} \right] \sin(X_8) \right] \tag{18}$$

$$\dot{X}_9 = \frac{I_y X_{12} - I_{yz} X_{11}}{I_y I_z - I_{yz}^2} + \cot(X_9) \left[\frac{X_{10}}{I_x} \sin(X_8) + \left[\frac{I_z X_{12} - I_{yz} X_{11}}{I_y I_z - I_{yz}^2} \right] \right] \tag{19}$$

$$\dot{X}_{10} = \left[\frac{I_y X_{12} - I_{yz} X_{11}}{I_y I_z - I_{yz}^2} \right] X_{11} - \left[\frac{I_z X_{11} - I_{yz} X_{12}}{I_y I_z - I_{yz}^2} \right] X_{12} + M_x \tag{20}$$

$$\dot{X}_{11} = \left[\frac{I_y X_{12} - I_{yz} X_{11}}{I_y I_z - I_{yz}^2} \right] X_{10} - \left[\frac{X_{10}}{I_x} \right] X_{12} + M_y \tag{21}$$

$$\ddot{X}_{12} = \left[\frac{I_z X_{11} - I_{yz} X_{12}}{I_y I_z - I_{yz}^2}\right] X_{10} - \left[\frac{X_{10}}{I_x}\right] X_{11} + M_z \tag{22}$$

The original version of the AVCO code uses a fifth order Runge-Kutta method with step-size control based on error estimates. However, the step-size is either doubled (if the computed error is less than a specified tolerance) or halved (if the computed error is greater than a specified tolerance). The rather arbitrary doubling or halving of the step-size can be inefficient because, for example, the step-size may be able to be greater than two, or it may not need to be halved, or doubling may cause the error to be too large, and then the another iteration is required, etc. It is more efficient to let the magnitude of the computed error control the step-size. The code was modified to use a time stepping method that computes the new step-size based on the computed truncation error. The new method incorporated into the code is general in the sense that any order Runge-Kutta method can be used. It is required only to input a table of coefficients specific to the order of the method. The Runge-Kutta method used was developed by Fehlberg [8]. The equations for a fifth order scheme are written for the variable X_j as:

$$f_{j_o} = f_j(X_{j_o}, t_o) \tag{23}$$

$$f_{j\kappa} = f_j\left(t_o + \alpha_\kappa dt, X_{j_o} + dt \sum_{\lambda = 0}^{\kappa} \beta_{\kappa\lambda} f_{j\lambda}\right) \quad \kappa = 0, 1, 2, 3, 4, 5 \tag{24}$$

$$X_j = X_{j_o} + dt \sum_{\kappa = 0}^{5} c_\kappa f_{j\kappa} + O(dt^6) \tag{25}$$

$$\hat{X}_j = X_{j_o} + dt \sum_{\kappa = 0}^{7} \hat{c}_\kappa f_{j\kappa} + O(dt^7) \tag{26}$$

The local truncation error is computed as,

$$(LTE)_j = X_j - \hat{X}_j = \sum_{\kappa = 0}^{7} (c_\kappa - \hat{c}_\kappa) f_{j\kappa} = O(dt^6) \tag{27}$$

The new step-size is computed based on the local truncation and is written as,

$$(dt)_{new} = (dt)_{old}\left(\frac{ERMAX}{(LTE)_{j, max}}\right)^{\frac{1}{5}} \tag{28}$$

where ERMAX is the maximum allowable error set by the user.

9

Although the above expressions are presented for a fifth-order scheme, the procedure is valid for any order scheme. The user needs only provide a set of, α_κ, $\beta_{\kappa\lambda}$, c_κ, and $\hat{c}_\kappa$. Sets of these coefficients for various order methods are presented by Fehlberg [8].

3.2 Modifications to Newtonian Regime Model

The original AVCO code uses a straight Newtonian method to compute the pressure distribution on each of the faces of the sabot in the Newtonian regime. However, straight Newtonian does not account for the effect of Mach number, and tends to over predict pressure near stagnation regions. Additionally, there is an inconsistency in the code because the actual side-face areas of a particular sabot are used to compute forces and moments in the interaction regime, whereas the side-face areas of the simple cylindrical shape shown in Figure 2 are used to compute the forces and moments in the Newtonian regime. This tends to cause an overprediction in the radial displacement after the sabot transitions to the Newtonian regime because the actual side-face area for a given sabot is generally less than that of the simple cylindrical shape shown in the figure.

The code was changed to use the modified Newtonian method for all Newtonian computations. Additionally, the same side-face areas used to compute the forces and moments in the interaction region are now used to compute the forces and moments in the Newtonian regime. This results in a better prediction of the radial displacement, especially at later times, as will be shown in Section 5.0.

3.3 New Front Scoop Geometry & Aerodynamic Model

The largest modification to the modeling was made to the front scoop geometry and associated aerodynamic model. The original version of the AVCO code modeled the front scoop with a simple conical shape. However, experimental designs under investigation today, for example the SLEKE sabot, use a ramp on the front scoop for structural support of the tip of the rod. There is no adequate way to model this geometry with the original AVCO code. Additionally, this geometry alters the aerodynamic flow field in the vicinity of the front scoop, and the flow field around this geometry is not modeled.

To model the front scoop with more than one line segment it was necessary to develop force and moment expressions for a line segment arbitrarily oriented with respect to the point O in Figure 5. The basic expressions for force and moment are given by:

$$\vec{F} = -\int_A P\hat{n} \, dA \qquad (29)$$

$$\vec{M} = \int_A P\hat{n} \times \vec{r} \, dA \qquad (30)$$

Where P is the pressure, $\hat{n}$ is the unit normal vector, and $\vec{r}$ is the moment arm from a suitably chosen reference point (in this case point "O"). For the front scoop $\hat{n}_j$ and $\vec{r}_j$ are given for line segment j, referring to Figure 5 as,
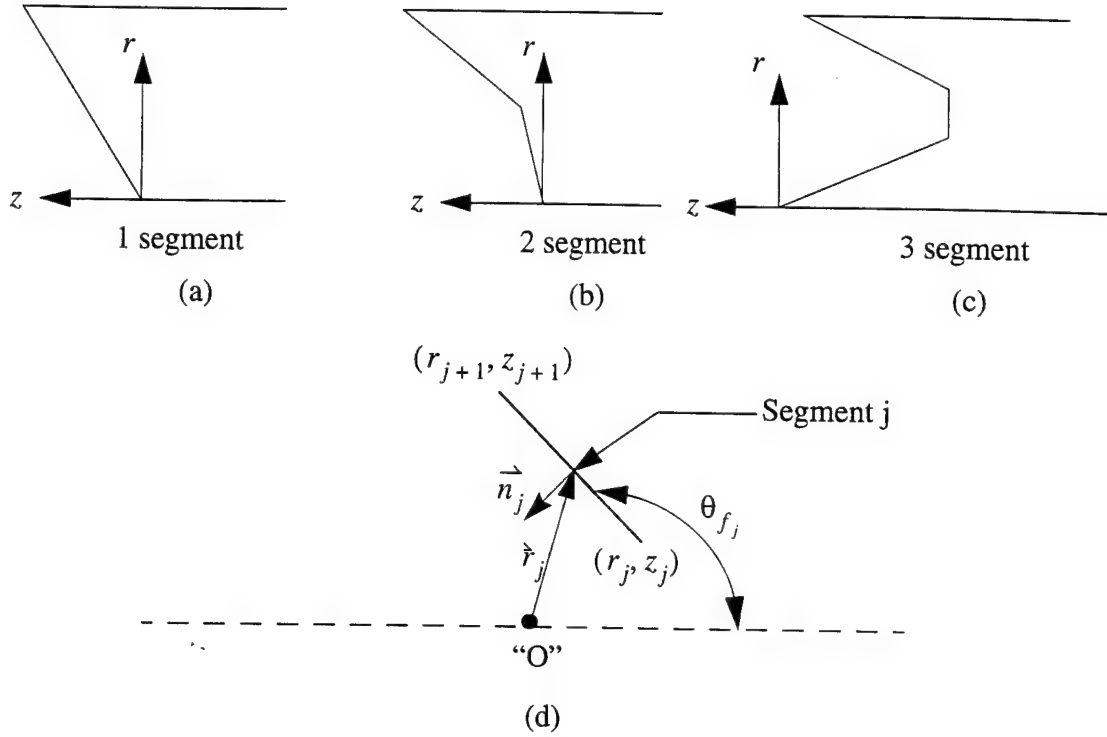
Figure 5.   New front scoop geometry model.

$$\hat{n}_j = \cos\theta_{f_j}\sin\phi\hat{i} + \cos\theta_{f_j}\cos\phi\hat{j} + \sin\theta_{f_j}\hat{k} \tag{31}$$

$$\hat{r}_j = r_j\sin\phi\hat{i} + r_j\cos\phi\hat{j} + z_j\hat{k} \tag{32}$$

In the interaction region there are two cases to consider. One is an attached shock configuration, where the pressure is assumed to be constant on the front scoop behind the shock. The other is a detached shock configuration, where the pressure is assumed to vary linearly in the radial direction over the front scoop.

For constant pressure, the forces and moments on segment j were derived to be:

$$F_{y_j} = -2P\sin\phi_o\left(\frac{r_{j+1}-r_j}{2}\right)\cot\theta_{f_j} \tag{33}$$

$$F_{z_j} = -2P\phi_o\left(\frac{r_{j+1}-r_j}{2}\right) \tag{34}$$

11

$$M_{x_j} = -2P\sin\phi_o \left[\frac{1}{\sin^2\theta_{f_j}} \left(\frac{r^3_{j+1} - r^3_j}{3} \right) \right.$$

$$\left. -\cot\theta_{f_j} (z_j + r\cot\theta_{f_j}) \left(\frac{r^2_{j+1} - r^2_j}{2} \right) \right] \tag{35}$$

For linearly varying pressure, the forces and moments on segment j were de   ed to be:

$$F_{y_j} = -\frac{2\cot\theta_{f_j}\sin\phi_o}{6(r_{j+1}-r_j)} \{ [r^3_{j+1} - r^2_j(3r_{j+1}-2r_j)]P_j \tag{36}$$

$$+ [r^2_{j+1}(2r_{j+1}-3r_j) + r^3_j]P_{j+1}\}$$

$$F_{z_j} = -\frac{2\phi_o}{6(r_{j+1}-r_j)} \{ [r^3_{j+1} - r^2_j(3r_{j+1}-2r_j)]P_j \tag{37}$$

$$+ [r^2_{j+1}(2r_{j+1}-3r_j) + r^3_j]P_{j+1}\}$$

$$M_{x_j} = -\frac{2\sin\phi_o}{12(r_{j+1}-r_j)\sin^2\theta_{f_j}} \{ [r^4_{j+1} + r^3_j(3r_j-4r_{j+1})]P_j \tag{38}$$

$$+ \left[r^4_j + r^3_{j+1}(3r_{j+1}-4r_j) \right]P_{j+1}\}$$

Finally, it was necessary to develop force and moment expressions for the front scoop in the Newtonian regime. This was done for a single segment in Crimi & Siegelman [2]. The components of force on segment j become:

$$F_{x_j} = -\rho_\infty (r^2_{j+1} - r^2_j) \cot\theta_{f_j} \left[V_z V_x \sin\theta\cos(\theta\phi_o - \sin\phi_o\cos\phi_o) \right. \tag{39}$$

$$\left. + \frac{2}{3}V_y V_x \cos^2\theta_{f_j}\sin^3\phi_o \right]$$

$$F_{y_j} = -\rho_\infty (r^2_{j+1} - r^2_j) \cot\theta_{f_j} \{ V^2_z\sin^2\theta_f\sin\phi_o + V_y V_z\sin\theta_{f_j}\cos\theta_{f_f}\phi_o \tag{40}$$

$$+ \sin\phi_o\cos\phi_o + \frac{1}{3}\cos\theta_{f_j} [V^2_y\sin\phi_o(2+\cos\phi_o) + V\sin\phi_o] \}$$

12

$$F_{z_j} = -\rho_\infty (r_{j+1}^2 - r_j^2) \left\{ \phi_o V_z^2 \sin^2\theta_{f_j} + 2V_y V_z \sin\theta_{f_j} \cos\theta_{f_j} \sin\phi_o \right. \tag{41}$$

$$\left. + \frac{1}{2}\cos^2\theta_{f_j} [V_y^2(\phi_o + \sin\phi_o\cos\phi_o) + V_x^2\sin^3\phi_o] \right\}$$

The expression for the moments are modified by an additional term due to a non-zero z_j. The expressions for the moments on segment j about point O become:

$$M_{x_j} = -2\rho_\infty \csc\theta_{f_j} \left[\frac{1}{3}(r_{j+1} - r_j) - \frac{r_j}{2}(r_{j+1}^2 - r_j^2)\cos^2\theta_{f_j} \right] \tag{42}$$

$$\{ V_z^2\sin\theta_{f_j}\sin\phi_o + V_y V_z\sin\theta_{f_j}\cos\theta_{f_j}(\phi_o + \sin\phi_o\cos\phi_o)$$

$$+ \frac{1}{3}\cos\theta_{f_j}[V_y^2\sin\phi_o(2 + \cos^2\phi_o) + V_x^2\sin^3\phi_o] \} - F_y z_j$$

$$M_{y_j} = -2\rho_\infty \csc\theta_{f_j} \left[\frac{1}{3}(r_{j+1} - r_j) - \frac{r_j}{2}(r_{j+1}^2 - r_j^2)\cos^2\theta_{f_j} \right] \tag{43}$$

$$V_x\cos\theta_{f_j} \left[\frac{2}{3}V_y\cos\theta_{f_j}\sin^3\phi_o + V_z\sin\theta_{f_j}\left(\phi_o - \frac{1}{2}\sin\phi_o\cos\phi_o\right) \right] + F_x z_j$$

The aerodynamic model associated with the new front scoop geometry is a combination of the constant pressure and linearly varying pressure cases described above. The specific combination depends on the number of line segments used to model the front scoop, the angle of attack of the sabot, and whether the flow on the underside of the sabot is choked based on 1-D inviscid gas dynamic relations.

For the two segment front scoop, two situations are considered. These situations are sketched in Figures 6 (a) and (b). At small angles of attack, an attached shock exists on the outer segment and a detached shock forms ahead of the inner segment. The pressure on the outer segment is assumed to be constant at the pressure behind the oblique shock. The pressure on the inner segment is assumed to vary linearly from stagnation conditions behind a normal shock corresponding to the conditions behind the oblique shock, to sonic conditions where the inner segment intersects the sabot underside. When the angle of attack is larger than for an oblique shock to exist on the outer segment, one detached shock is assumed to exist and the pressure is assumed to vary linearly from stagnation at the outer radius of the sabot to sonic at the inner radius.

For the three segment front scoop, the pressure on each segment of the front scoop is assumed to be uniformly at stagnation conditions behind a normal shock corresponding to the incoming freestream conditions.

4.0 ANALYTICAL MODEL

In order to help verify the trends predicted by the AVCO code, a simple analytical model was developed. These results are compared to results predicted by the AVCO code. A schematic of the analytical model is shown in Figure 7.
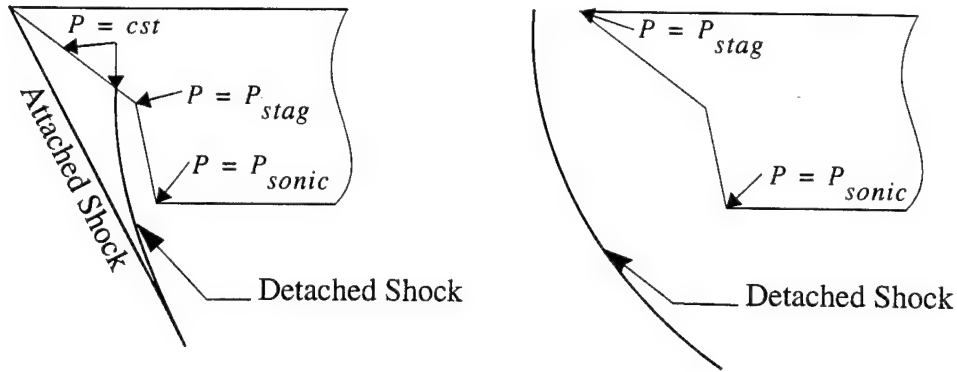
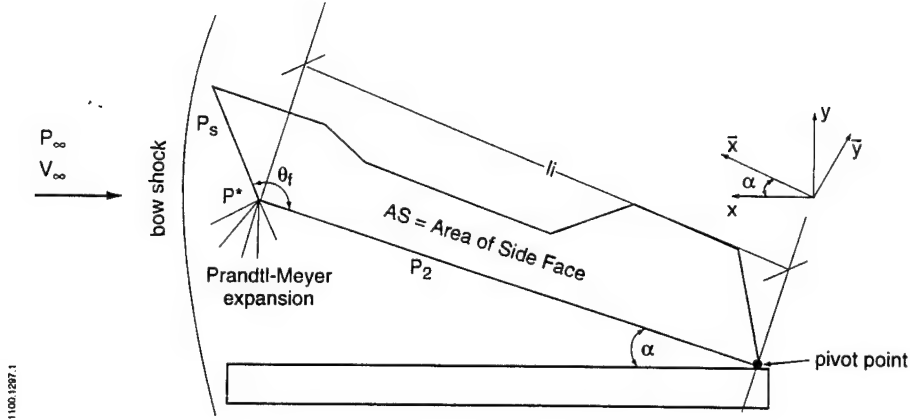**Figure 6. Two segment aerodynamic model.**

Figure 7. Analytical model.

The model assumes that the pressure on the front scoop is the stagnation pressure behind a normal shock corresponding to the freestream Mach number. This relationship is well known and is given by,

$$P_o = P_\infty \left[\frac{(\gamma + 1) M_\infty^2}{2} \right]^{\frac{\gamma}{\gamma - 1}} \left[\frac{(\gamma + 1)}{2\gamma M_\infty^2 - (\gamma - 1)} \right]^{\frac{1}{\gamma - 1}} \tag{44}$$

It is assumed that the pressure on the front scoop is uniformly at stagnation pressure and that the flow at the corner point where the front scoop intersects the underside of the sabot is at sonic conditions corresponding to an isentropic expansion from the conditions behind the normal shock. The flow then turns through a Prandtl-Meyer expansion around the corner. Since it is assumed that

14

the conditions at the corner are sonic, the Prandtl-Meyer function on the underside is simply $\nu(M_2) = \pi - \theta_f$. Knowing the value of ν, the Mach number after the Prandtl-Meyer expansion is determined. The static pressure, P_2, is then determined from,

$$\frac{P^*}{P_2} = \left[\frac{1 + \frac{\gamma-1}{2}M_2^2}{1 + \frac{\gamma-1}{2}} \right]^{\frac{\gamma}{\gamma-1}} \qquad (45)$$

where P^* is the pressure corresponding to sonic conditions.

With the above pressures acting on the front scoop and underside of the sabot, the forces and moments acting on the sabot petal are summed assuming that the sabot pivots about the aft end. Summing moments and applying $M_t = I_{\bar{x}}d^2\alpha/dt^2$ the equation for rotation is obtained as,

$$\frac{d^2\alpha}{dt^2} = \frac{1}{I_{\bar{x}}} \left[\frac{P_o \sin\phi_o}{\sin^2\theta_f} \left(\frac{r_o^3 - r_i^3}{3} \right) + (r_i\cot\theta_f + l_i)F_{\bar{y}_f} + P_2 \sin\phi_o A_s l_i \right] \qquad (46)$$

The expression in the brackets is the total moment M_t about the sabot petal tail, and the entire expression on the right hand side is a function of the sabot geometry and the freestream conditions. The term $F_{\bar{y}_f}$ is the same as given by equation (33). The entire right hand side expression is constant for a given geometry and freestream conditions so the equation can be easily integrated twice to obtain an expression for the angular velocity and angular displacement of the sabot petal as a function of time. The resulting equation is converted to a function of down range position by introducing the projectile velocity into the equation, i.e., $t = x/V_p$. The resulting equation is simply,

$$\alpha(x) = \frac{M_t x^2}{2I_{\bar{x}}V^2} \qquad (47)$$

Next, the forces in the y direction are summed to obtain an expression for the radial displacement of the sabot as a function of down range position x. Summing forces yields:

$$\frac{d^2 r}{dt^2} = \frac{2\sin\phi_o}{m}\left[(r_i l_i + A_s)P_2 - P_o\left(\frac{r_o^2 - r_i^2}{2}\right)\cot\theta_f\right]\cos\left(\frac{M_t x^2}{2I_{\bar{x}}V^2}\right)$$

$$- 2P_o\phi_o\left(\frac{r_o^2 - r_i^2}{2}\right)\sin\left(\frac{M_t x^2}{2I_{\bar{x}}V^2}\right)$$

<div align="right">(48)</div>

The expression for angle of attack, α, from equation (47) has been inserted into (48). This equation can be integrated twice to obtain an expression for the radial displacement as a function of position. However, to integrate the equation, the sine and cosine terms must be written in terms of their series expansions. The resulting expression for radial displacement is written as:

$$r(x) = \frac{2\sin\phi}{mV^2}\left[(r_i l_i + A_s)P_2 - P_o\left(\frac{r_o^2 - r_i^2}{2}\right)\cot\theta_f\right]$$

$$\left[\sum_{n=0}^{\infty}\frac{(-1)^n}{(2n)!}\left(\frac{M_t x^2}{2I_{\bar{x}}V^2}\right)^{2n}\frac{x^2}{(4n+1)(4n+2)}\right]$$

<div align="right">(49)</div>

$$-2P_o\phi_o\left(\frac{r_o^2 - r_i^2}{2}\right)\sum_{n=0}^{\infty}\frac{(-1)^n}{(2n+1)!}\left(\frac{M_t x^2}{2I_{\bar{x}}V^2}\right)^{2n+1}\frac{x^2}{(4n+3)(4n+4)}$$

5.0 NUMERICAL RESULTS

The modified version of the AVCO code was used to compute the sabot separation trajectories for three IAT sabots. The results are compared to experimental data obtained in the IAT's Hypervelocity Launch Facility. The results of the analytical model are also presented and compared to the experimental data and to the results computed by the AVCO code. Overall, there was good agreement between the experimental data and the results computed by the AVCO code. Furthermore, there was surprisingly good agreement between the results computed by the analytical model and the experimental data, considering the simplicity of the analytical model.

The IAT sabots are shown in Figures 8 (a) through (c) and are referred to as the HVP_009, HVP_015, and HVP_016 sabots, respectively. The HVP_009 and HVP_015 sabots are similar, the primary difference being the axial location of the center of mass. The front scoop on these sabots is adequately modeled with two line segments. The primary difference between the HVP_016 sabot and the other two is the addition of a forward ramp on the front scoop. This geometry is modeled with three line segments.
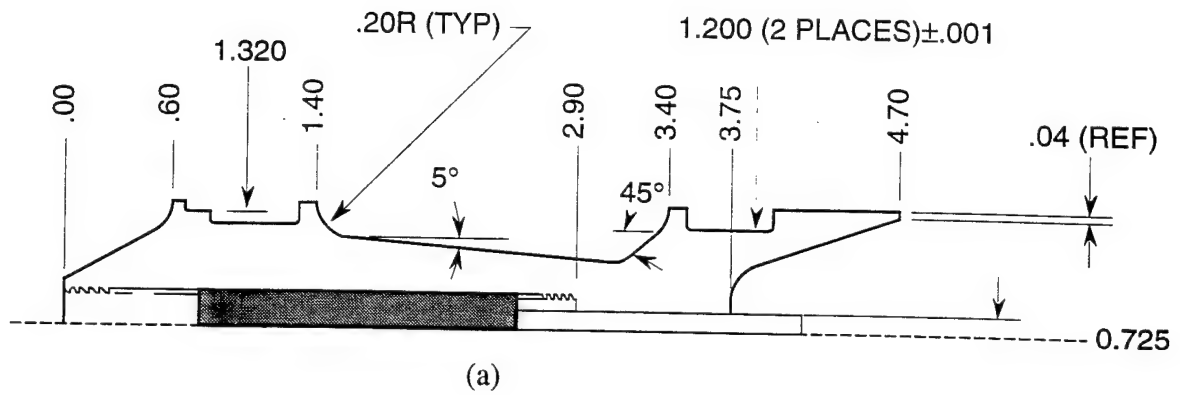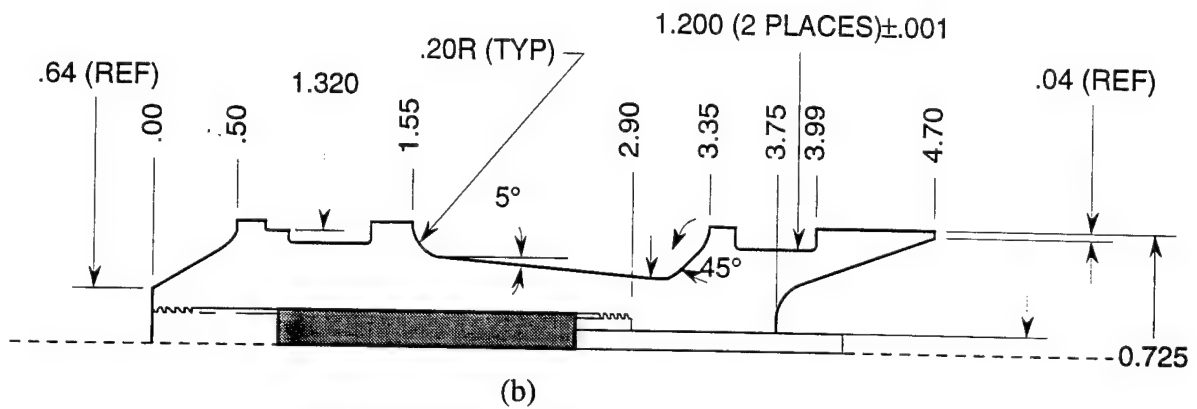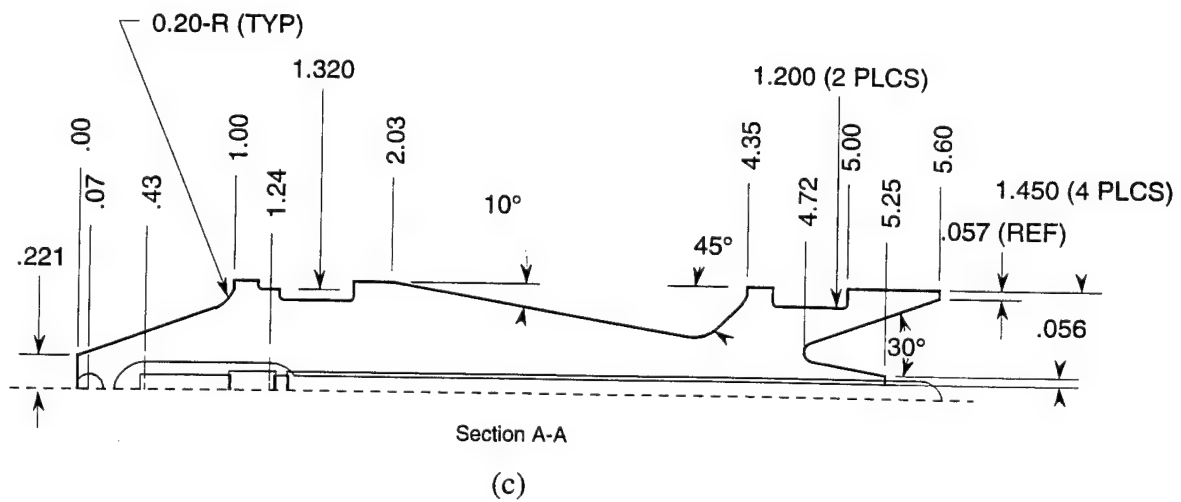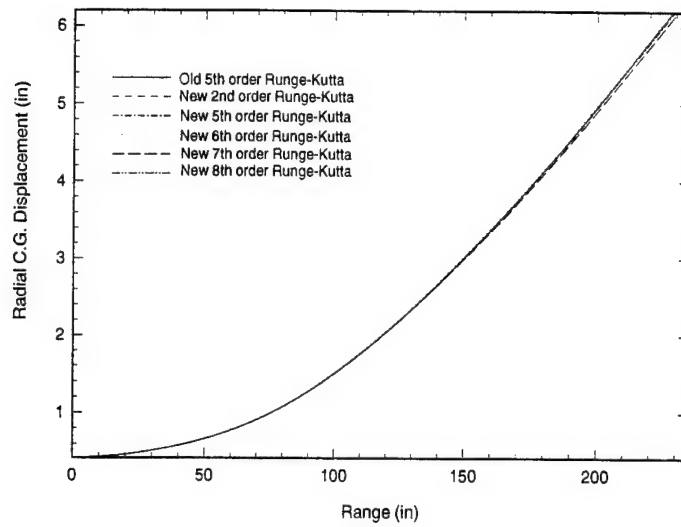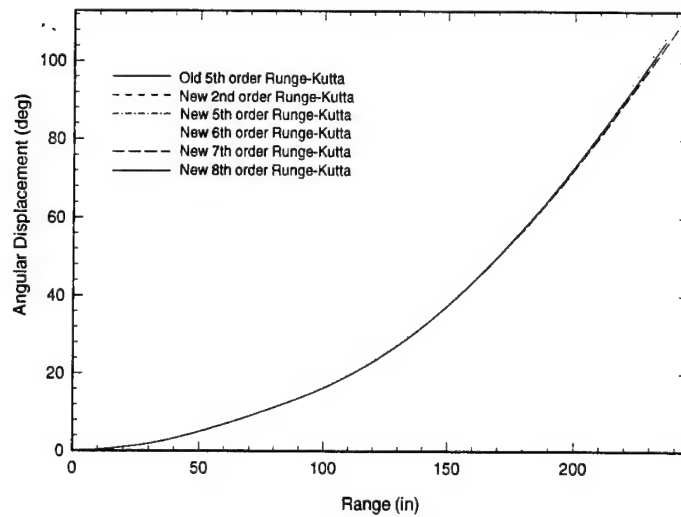
16

Figure 8. IAT sabot models.

17

(a)

(b)

Figure 9. **Radial (a) and angular (b) displacement computed by new and old Runge-Kutta time stepping schemes.**

Before the modified code was used to predict sabot trajectories, the new Runge-Kutta and time stepping algorithm were compared to the old algorithm to insure that the new scheme was working properly and producing accurate results.

Figures 9 (a) and (b) show the radial and angular displacements, respectively, for the HVP_009 sabot computed using both the original and new Runge-Kutta and time stepping schemes. As previously mentioned, the original code uses a 5th order scheme. The results using the new scheme are presented using 2nd, 5th, 6th, 7th, and 8th order schemes. As seen in the figure, the results computed by the new scheme agree with the results computed using the old

scheme, indicating that the new scheme is producing accurate results. It should be noted that the old 5th order scheme took 189 time steps to compute the solution compared to 125, 141, 152, 188, and 139 time steps for the new 2nd, 5th, 6th, 7th, and 8th order schemes, respectively, so the new scheme computes the solution in less time steps than the old one. The results indicate that the 2nd order scheme may be the most preferable since it not only uses the fewest number of time steps, but also performs the fewest computations per time step.

Next the code was run for the three IAT sabots to determine the overall accuracy of the code on a variety of sabot geometries, and to assess the improvements made to the original version of the code. The results are presented and discussed in the following paragraphs along with the results of the analytical model.

The HVP_009 sabot and HVP_015 sabot are geometrically very similar. The front scoops on these two sabots are adequately modeled by two line segments. With the old version of the code, the front scoops would be modeled as one straight line segment from the outer to the inner radius.

Both the modified and original versions of the code were used to compute the radial and angular separation, and these results were compared to the experimental data to determine the relative performance of each version of the code. The experimental data were taken at range pressures of 380 torr for the HVP_009 sabot and at 380 torr and 430 torr for the HVP_015 sabot. The computed and experimental radial and angular displacements are shown in Figures 10 (a) and (b) for the HVP_009 sabot, and in Figures 11 (a) and (b) (370 torr) and in Figures 12 (a) and (b) (430 torr) for the HVP_015 sabot.

In all cases, the modified version of the code computes the radial displacements more accurately than the original version. Remarkably, the simple analytical model predicts the radial displacements more accurately than either version of the code. The angular displacements computed by the modified and original version of the code are nearly the same, and both predict the angular displacements accurately. However, the analytical model does not predict the angular displacements as well as the AVCO code.

The computed and experimental results for the HVP_016 sabot are shown in Figures 13 (a) and (b). This sabot was not modeled using the original version of the code because there is no way to adequately model the front scoop geometry of this sabot with the original version of the code. The results show the same general trends as the HVP_009 and HVP_015 sabots, with the computed results slightly overpredicting the radial displacement while correctly predicting the angular displacement and the analytical model more accurately predicting the radial displacement while somewhat overpredicting the angular displacement.
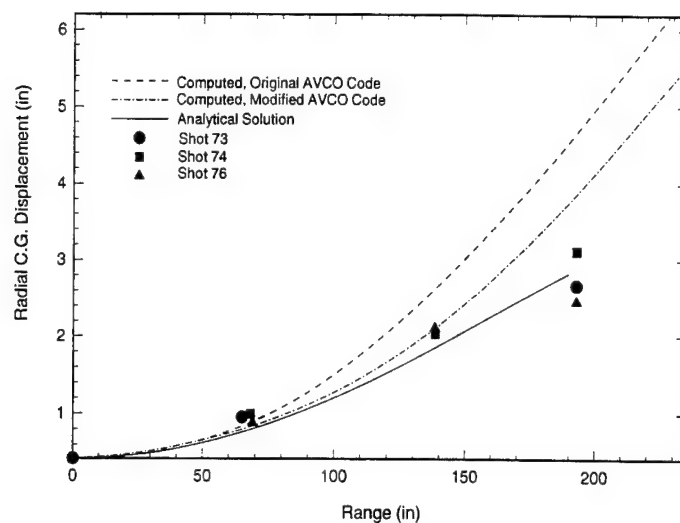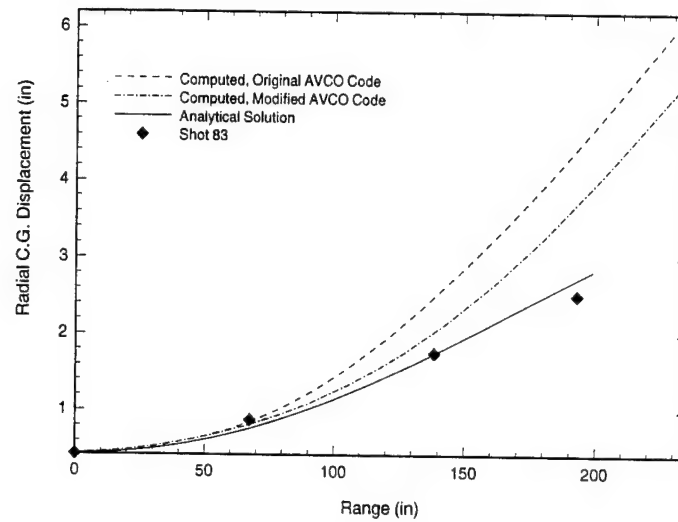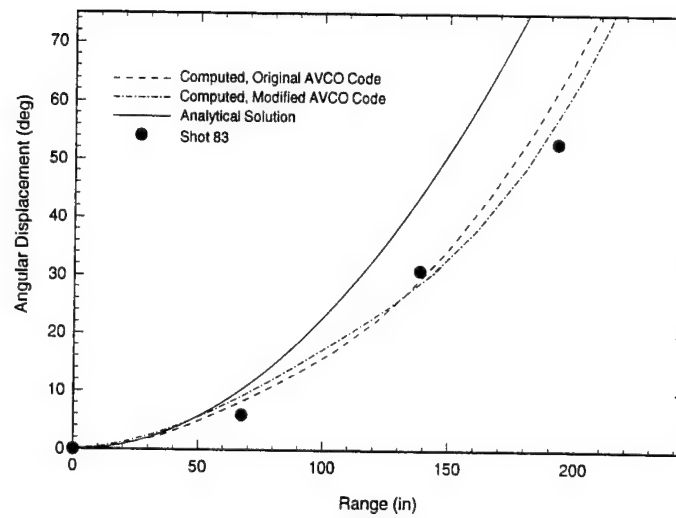
(a)
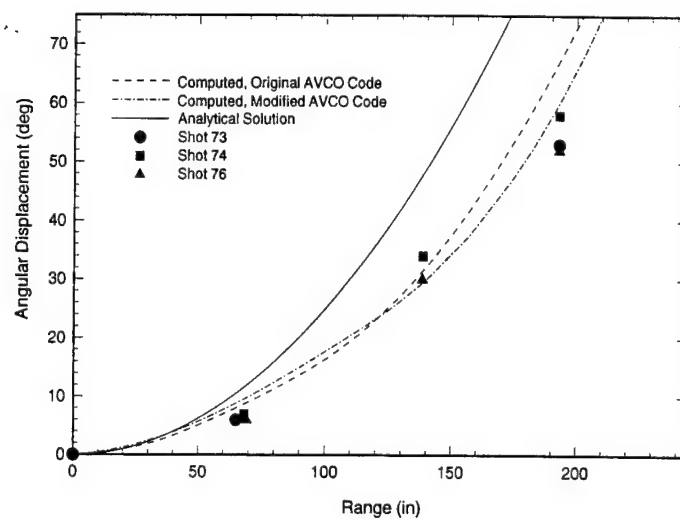
(b)

Figure 10. Computed and experimental radial (a) and angular (b) displacements, HVP_009 sabot, 380 torr.
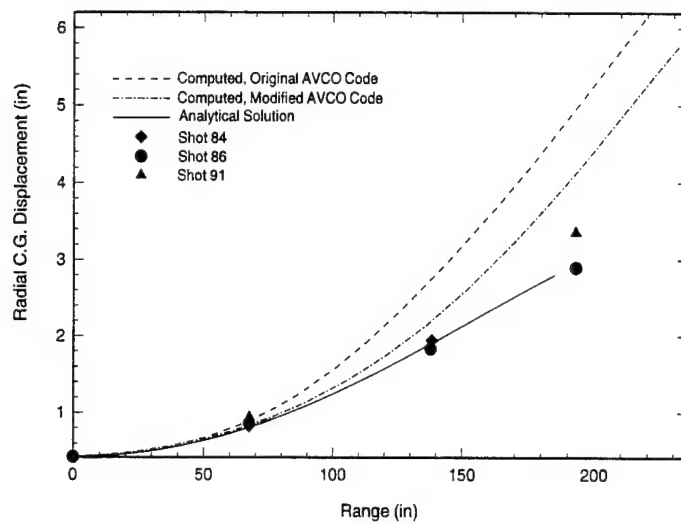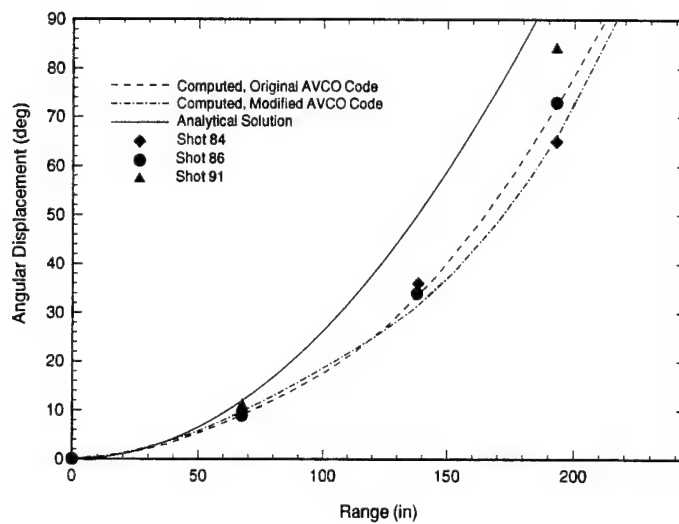
20

(a)

(b)

Figure 11. Computed and experimental radial (a) and angular (b) displacements, sabot HVP_015, 370 torr.

(a)

(b)

Figure 12.   Computed and experimental radial (a) and angular (b) displacements, sabot
HVP_015, 430 torr.

22
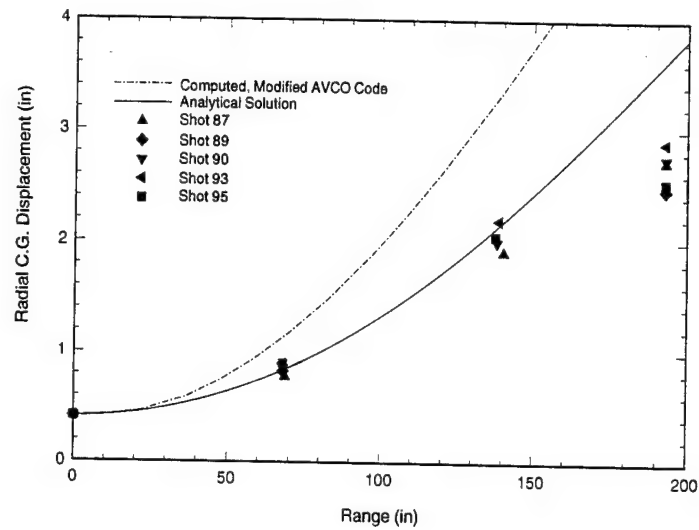
(a)
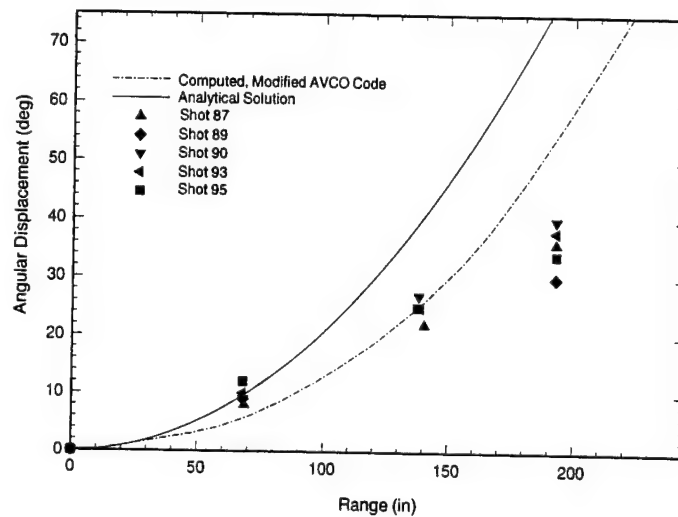
(b)

Figure 13. Computed and experimental radial (a) and angular (b) displacements, sabot HVP_016, 500 torr.

6.0   USING THE MODIFIED CODE

The changes in the input file for the modified code are relatively minor and relate only to the specification of the front scoop geometry. Table 1 shows the portion of the original and modified code input files up to the specification of the side-face areas. On line four, the front scoop angle (150.0) has been removed and replaced with three additional lines just before the specifica-

tion of the side-face areas. The first line contains the number of segments used to de   :ibe +)
front scoop geometry, in this case two. The second line gives the angle of each segment   ing
original definition of the front scoop angle. The third line gives the radial location of t   in:
most end of each segment. These are the only modifications to the input files needed f   un
modified version of the code, all other changes are internal to the code. The code (ir   .f)   :
creates an input file interactively from user keyboard input has also been modified to   .ept   :
new front scoop geometry definitions.

Table 1. Sample Input, Original and Modified Code

Original Code Input

```
3.1251730000000002E-03  3.8773870000000003E-05  3.9285970000000001E-05
1.4176770000000000E-06  8.8792139999999992E-07  1.0000000000000001E-05
5.0000000000000002E-05  3.5299999999999998E-02  0.0000000000000000E+00
0.0000000000000000E+00  2.2500000000000000E-03  1.0000000000000000E-05
45.00000000000000      137.0000000000000   150.0   0.312500000000000
0.341670000000000
9.8750000000000001E-03  5.7083000000000002E-02  0.15
8530.100000000000      0.1909916700000000      -2000.000000000000
1.0000000000000001E-04  1.0000000000000000E-04   0.083875
0.0000000000000000E+00  100000000.0000000       100000000.0000000
100000000.0000000       100000000.0000000      1.0000000000000000E-04
0.0000000000000000E+00  7.9000000000000006E-06  0.1083330000000000
-0.1909916700000000      1.400000000000000       1030.150000000000
1.1519171000000000E-03  1120.000000000000       1.000000000000000
     0      1      1      0      0      5
     0      0      1      0      0      0
     0
```

Modified Code Input

```
3.1251730000000002E-03  3.8773870000000003E-05  3.9285970000000001E-05
1.4176770000000000E-06  8.8792139999999992E-07  1.0000000000000001E-05
5.0000000000000002E-05  3.5299999999999998E-02  0.0000000000000000E+00
0.0000000000000000E+00  2.2500000000000000E-03  1.0000000000000000E-05
45.00000000000000      137.0000000000000      0.312500000000000
0.341670000000000
9.8750000000000001E-03  5.7083000000000002E-02   0.15
8530.100000000000      0.1909916700000000      -2000.000000000000
1.0000000000000001E-04  1.0000000000000000E-04   0.083875
0.0000000000000000E+00  100000000.0000000       100000000.0000000
100000000.0000000       100000000.0000000      1.0000000000000000E-04
0.0000000000000000E+00  7.9000000000000006E-06  0.1083330000000000
-0.1909916700000000      1.400000000000000       1058.000000000000
1.1830500000000000E-03  1120.000000000000       1.000000000000000
     0      1      1      0      0      5
     0      0      1      0      0      0
     0
     2
90.00000000000000      160.0000000000000
9.8750000000000001E-03  2.8267000000000000E-02  5.7083000000000002E-02
```

24

7.0   CONCLUSIONS & RECOMMENDATIONS

Several modifications were made to the AVCO code in an attempt to improve its accuracy and to allow the code to compute the separation of more complex sabot geometries. The two most significant modifications were changing the code to use the same side-face areas to compute forces and moments in the Newtonian regime as are used in the interaction regime, and incorporating a new front scoop geometry and associated aerodynamic model into the code. The first modification results in an improved prediction of the radial displacement over the original version of the code, whereas the second allows the code to be used to compute trajectories of more complex sabot designs.

The results indicate improved predictions over the original version of the code. The angular displacements were predicted very well. However, the code still tends to overpredict the radial displacements in all cases computed, although not as greatly as the original version of the code. This indicates that further refinements to the aerodynamic model, specifically the underside pressure model, may be needed.

It is interesting to note that the analytical model predicted the radial displacements very well in all cases. This may give a clue as how to refine the aerodynamic model in the code. The forces computed with the analytical model and the AVCO code are very similar except in one respect. It was previously discussed that the AVCO code incorporates a "pressure pulse" model into the side-face area and underside force computations based on the fact that previous experiments by Schmidt [7], on sabots of the type shown in Figure 2, indicate that a pressure pulse occurs on the underside and side-face areas of the sabot due to shock reflections and interactions. The procedure developed by Crimi & Siegelman [2], approximates the pressure distribution using an empirical procedure. The pressure pulse predicted by this procedure was compared to the experimental data by Schmidt [7], and shown to provide acceptably accurate results. However, it must be noted that this procedure was applied to sabots with simple conical front scoops as shown in Figure 5 (a) and compared to data taken using like sabots. However, it is not known what effect front scoops of the type shown in Figures 5 (b) and (c) have on the magnitude and distribution of the pressure pulse. If the effect of the different front scoop geometries is to diminish the pressure pulse, then it is possible that the code predicts the angular displacement well and not the radial displacement because the pressure pulse incorporated into the code causes a net increased lifting force in the radial direction. But if the pulse is centered, or nearly centered, about the sabot center of gravity, then the moments produced by the forces on either side of the center of gravity tend to cancel each other, thereby having little or no effect on the angular displacement.

In order to investigate the effect of the different front scoop geometry and to test the hypothesis stated above, an experimental program on the sabot shown in Figure 8 (c) has been initiated. The experimental program will be carried out in the Mach 5 blowdown wind tunnel at The University of Texas at Austin. Detailed pressure measurements on the front scoop, underside, and side-face areas of the sabot will be made to determine whether a pressure pulse exists for this geometry and, if so, how well the current procedure in the AVCO code predicts its shape and magnitude. The data will be used to modify the pressure pulse model in the AVCO code, if necessary. This will be documented in a subsequent report.

25

ACKNOWLEDGMENTS

REFERENCES

[1] Crimi, P. & Siegelman, D., Analysis of Mechanical and Gasdynamic Loadings Duri   abot Discard From Gun-Launched Projectiles, BRL-CR 341 Report, June 1977.

[2] Crimi, P. & Siegelman, D. Projectile/Sabot Discard Aerodynamics, BRL-CR-00410, December 1979.

[3] Siegelman, D., Wang, J., Sabot Design Optimization, ARBRL-CR-00450, March 1981.

[4] Siegelman, D., Wang, J., Crimi, P., Computation of Sabot Discard, ARBRL-CR-00505, February 1983.

[5] Savik, Douglas, AVCO Sabot Discard Program, BRL, Launch and Flight Division, Fluid Mechanics Branch, 1986, not published.

[6] Sepri, Paavo, Aerodynamic Interaction Between Projectile Fins and Sabot Petals, Contract No. DAAG29-81-D0100, Delivery Order 2359, September 1986.

[7] Schmidt, E., Wind Tunnel Measurements of Sabot Discard Aerodynamics, ARBRL-TR-02246, July 1980.

[8] Fehlberg, Erwin, Classical fifth-, sixth-, seventh-, and eighth-order Runge-Kutta formulas with step-size control, NASA TR R-287, 1968.

APPENDIX

Table 2. HVP_009 Geometric Input Data

Input Parameters				Side Face Areas & Centroids	
EBAR (ft)	0.0353	ZBASE(ft)	-0.190992	X_2 (ft^2)	-0.0475498
SPIN (rad/s)	0	EM (slug)	0.003125	Y_2 (ft)	0.0249896
PHIZ (DEG)	45	XOFF(ft)	0.083875	A_3 (ft^2)	0.0014009
THETB(DEG)	137	**Moment of Inertia**		X_3 (ft)	-0.1061320
THETF1 (DEG)	90	I_{xx} (slug-ft^2)	3.877387×10^{-5}	Y_3 (ft)	0.0268358
THETF2 (DEG)	160	I_{yy} (slug-ft^2)	3.928597×10^{-5}	A_4 (ft^2)	0.0015603
THETF3 (DEG)		I_{zz} (slug-ft^2)	1.417677×10^{-6}	X_4 (ft)	-0.1687210
R1 (ft)	0.009875	I_{yz} (slug-ft^2)	8.879214×10^{-7}	Y_4 (ft)	0.0301209
R2 (ft)	0.028267	**Side Face Areas & Centroids**		A_5 (ft^2)	0.0039566
R3 (ft)	0.057083	A_1 (ft^2)	0.0029034	X_5 (ft)	-0.2426124
R4(ft)		X_1 (ft)	0.0065799	Y_5 (ft)	0.0358399
ZBAR (ft)	0.190992	Y_1 (ft)	0.0420632		
ZSEP (ft)	0.108333	A_2 (ft^2)	0.0011944		

Table 3. HVP_015 Geometric Input Data

Input Parameters		Input Parameters		Side Face Areas & Centroids	
EBAR (ft)	0.0359	ZBASE(ft)	-0.1857	X_2 (ft^2)	-0.0500422
SPIN (rad/s)	0.0	EM (slug)	0.0034	Y_2 (ft)	0.0254548
PHIZ (DEG)	45.0	XOFF(ft)	0.0793	A_3 (ft^2)	0.0014265
THETB(DEG)	131.0	**Moment of Inertia**		X_3 (ft)	-0.1049998
THETF1 (DEG)	90.0	I_{xx} (slug-ft^2)	4.4202127×10^{-5}	Y_3 (ft)	0.0273330
THETF2 (DEG)	160	I_{yy} (slug-ft^2)	4.261402×10^{-5}	A_4 (ft^2)	0.0013050
THETF3 (DEG)		I_{zz} (slug-ft^2)	1.567513×10^{-6}	X_4 (ft)	-0.1161451
R1 (ft)	0.00988	I_{yz} (slug-ft^2)	7.822864×10^{-7}	Y_4 (ft)	0.0304434
R2 (ft)	0.02827	**Side Face Areas & Centroids**		A_5 (ft^2)	0.0047971
R3 (ft)	0.05708	A_1 (ft^2)	0.0031140	X_5 (ft)	-0.2390058
R4(ft)		X_1 (ft)	0.0040216	Y_5 (ft)	0.0365371
ZBAR (ft)	0.18570	Y_1 (ft)	0.0415954		
ZSEP (ft)	0.10833	A_2 (ft^2)	0.0011181		

Table 4. HVP_016 Geometric Input Data

Input Parameters				Side Face Areas & Centroids	
EBAR (ft)	0.03420	ZBASE(ft)	0.23173	X_2 (ft²)	-0.0128333
SPIN (rad/s)	0.0	EM (slug)	0.00427	Y_2 (ft)	0.0245161
PHIZ (DEG)	45.0	XOFF(ft)	0.01572	A_3 (ft²)	0.0040538
THETB(DEG)	154.0	**Moment of Inertia**		X_3 (ft)	-0.2237487
THETF1 (DEG)	10.0	I_{xx} (slug-ft²)	6.41473×10^{-5}	Y_3 (ft)	0.0310484
THETF2 (DEG)	90.0	I_{yy} (slug-ft²)	6.472449×10^{-5}	A_4 (ft²)	0.0041887
THETF3 (DEG)	160.0	I_{zz} (slug-ft²)	1.959655×10^{-6}	X_4 (ft)	-0.3100515
R1 (ft)	0.01420	I_{yz} (slug-ft²)	1.016722×10^{-6}	Y_4 (ft)	0.0359374
R2 (ft)	0.02105	**Side Face Areas & Centroids**		A_5 (ft²)	0.0021168
R3 (ft)	0.03092	A_1 (ft²)	0.0032944	X_5 (ft)	-0.3927413
R4(ft)	0.05567	X_1 (ft)	-0.0382089	Y_5 (ft)	0.0224234
ZBAR (ft)	0.23173	Y_1 (ft)	0.0384661		
ZSEP (ft)	0.21491	A_2 (ft²)	0.0028290		

Distribution List

Administrator
Defense Technical Information Center
Attn: DTIC-DDA
8725 John J. Kingman Road, Ste 0944
Ft. Belvoir, VA 22060-6218

Director
US Army Research Lab
ATTN: AMSRL OP SD TA
2800 Powder Mill Road
Adelphi, MD 20783-1145

Director
US Army Research Lab
ATTN: AMSRL OP SD TL
2800 Powder Mill Road
Adelphi, MD 20783-1145

Director
US Army Research Lab
ATTN: AMSRL OP SD TP
2800 Powder Mill Road
Adelphi, MD 20783-1145

Director
Army Research Laboratory
AMSRL-CI-LP
Technical Library 305
APG, MD 21005-5066